







Cite this: *Phys. Chem. Chem. Phys.*, 2025, 27, 24948

# Probing binding-site preferences in a propiolic acid complex with water at 0.4 K

Arghya Chakraborty,  Stefan Henkel,  Gerhard Schwaab  and Martina Havenith \*

Carboxylic acid···water complexes serve as model systems for understanding molecular interactions that are fundamental to bio- and atmospheric chemistry. Utilizing the helium nanodroplet (HND) technique, which enables the kinetic trapping of otherwise inaccessible isomeric structures, we investigated the hydrogen bonding site preferences in a 1:1 complex of propiolic acid ( $\text{HC}\equiv\text{C}-\text{COOH}$ , PA) with  $\text{D}_2\text{O}$ . Mass-selective infrared (IR) spectra recorded in the  $\text{C}=\text{O}$  and  $\text{C}\equiv\text{C}$  stretching regions confirmed the exclusive isolation of the *cis*-PA conformer under single-molecule doping conditions of the helium droplets. Further complexation of PA with  $\text{D}_2\text{O}$  inside the droplets yielded three distinct isomers of *cis*-PA··· $\text{D}_2\text{O}$  dimer, with the dominant spectral features corresponding to two kinetically trapped structures stabilized by either a non-classical ( $\equiv\text{C}-\text{H}\cdots\text{OD}_2$ ) or a classical ( $\text{C}=\text{O}\cdots\text{DOD}$ ) hydrogen bond. A weak IR band corresponding to the global minimum isomer, characterized by a six-membered ring involving  $\text{D}_2\text{O}$  and the  $\text{COOH}$  moiety, is also observed. The structural assignments are aided by harmonic IR spectra of the lowest-energy isomers of PA··· $\text{D}_2\text{O}$  complexes computed at the MP2/aug-cc-pVDZ level. These structural findings demonstrate the balance of the dipole–dipole and higher-order interactions in steering aggregation dynamics in HNDs. Notably, the polar  $\text{D}_2\text{O}$  ( $\mu = 1.85$  D) and PA ( $\mu = 1.59$  D) promote directional association leading to the formation of local minimum structures, which are lying  $>20$   $\text{kJ mol}^{-1}$  above that of the global minimum isomer. The calculated interconversion energy barriers for *cis*-PA··· $\text{D}_2\text{O}$  isomers are in accordance with kinetic trapping inside HNDs at 0.4 K.

Received 22nd July 2025,  
Accepted 13th October 2025

DOI: 10.1039/d5cp02794b

rsc.li/pccp

## 1. Introduction

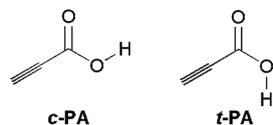
Hydrogen bonds (HBs) have been a topic of discussion since their discovery,<sup>1</sup> as they play pivotal roles in various chemical and physical processes across the liquid, solid and gas-phases.<sup>2–4</sup> Beyond their well-established significance in general chemistry or biological systems,<sup>3,5,6</sup> a molecular understanding of hydrogen bonding is pivotal for supramolecular chemistry,<sup>7</sup> atmospheric chemistry,<sup>8</sup> mineralogy,<sup>9</sup> and materials science.<sup>10–12</sup> HBs were considered classically to be formed between two substantially electronegative atoms with a hydrogen atom in between ( $\text{X}-\text{H}\cdots\text{Y}$ ) where one atom acts as the HB donor (X) and the other as the acceptor (Y).<sup>13</sup> In the last few decades, low-temperature experiments supported by theoretical studies have greatly reshaped the understanding of HB interaction.<sup>14–20</sup> For instance, C–H or  $\pi$ -electrons have been recognized as actively participating in HB formation.<sup>3,21,22</sup> Although weaker in strength, these non-classical hydrogen bonds play a crucial role in stabilizing the three dimensional structures of biomolecules,<sup>5</sup> crystal packing of chemical

compounds,<sup>23</sup> and the nucleation and growth of atmospheric aerosol particles.<sup>8</sup>

In this context, helium nanodroplets (HNDs) offer a unique and highly versatile medium for exploring unconventional intermolecular interactions, particularly through the stabilization of binary complexes. In contrast to gas-phase techniques (*e.g.* molecular beam experiments)<sup>24–26</sup> and solid-phase methods (*e.g.* matrix isolation),<sup>27,28</sup> which predominantly favor the stabilization of global minimum structures, HNDs often enable the stabilization of local minimum configurations that are otherwise challenging to access.<sup>29</sup> This distinctive capability arises primarily from the intrinsic properties of HNDs, the ultracold temperature ( $\sim 0.4$  K) and the superfluid nature.<sup>30</sup> The formation mechanism of molecular complexes within HNDs is governed by the sequential pickup of molecules with each undergoing rapid thermalization to its vibrational ground state prior to complexation. In the case of polar molecules, the long-range dipole–dipole force guides the orientation and approach of the molecules during aggregation.<sup>30</sup> It is consistently supported by experimental studies involving a broad range of systems—including homodimeric, trimeric and oligomeric clusters such as dimers of formic acid,<sup>31</sup> acetic acid,<sup>32</sup> pyruvic acid,<sup>33</sup> ( $\text{OCS}$ )<sub>3</sub>,<sup>34</sup> cyclic water hexamers [cyclic-( $\text{H}_2\text{O}$ )<sub>6</sub>],<sup>35</sup>

Lehrstuhl für Physikalische Chemie II, Ruhr-Universität Bochum, 44801 Bochum, Germany. E-mail: [martina.havenith@rub.de](mailto:martina.havenith@rub.de)





**Scheme 1** Schematic diagram of the *cis* and *trans* isomers of propiolic acid (PA). The acronyms **c-PA** and **t-PA** are elaborated in Section 2.3.

and hydrogen cyanide  $[(\text{HCN})_n]$  chains.<sup>29</sup> Similar trends have been observed in heterodimeric systems, which can be exemplified by the propargyl alcohol  $\cdot\cdot\text{D}_2\text{O}$  complex. Here, two local minimum structures located approximately 5 and 13  $\text{kJ mol}^{-1}$  above the global minimum have been identified.<sup>36</sup>

Carboxylic acids bearing additional functional groups present a rich landscape of hydrogen-bonding motifs due to the presence of multiple HB donors and acceptors. Propiolic acid ( $\text{HC}\equiv\text{C}-\text{COOH}$ , PA), which contains a carboxylic ( $-\text{COOH}$ ) and an acetylenic ( $-\text{C}\equiv\text{CH}$ ) moiety, exemplifies such a multifunctional system. Precisely, in PA the  $\text{C}\equiv\text{C}$   $\pi$ -electrons, the carbonyl oxygen ( $\text{C}=\text{O}$ ), and the hydroxyl oxygen ( $\text{O}-\text{H}$ ) serve as HB acceptors, while the acetylenic hydrogen ( $\text{H}-\text{C}\equiv$ ) and hydroxyl hydrogen ( $-\text{OH}$ ) act as HB donors. Scheme 1 presents two planar configurations of PA: *cis* (**c-PA**) and *trans* (**t-PA**). The global minimum species **c-PA** characterized by a  $0^\circ$  dihedral angle ( $\text{O}=\text{C}-\text{O}-\text{H}$ , along  $\text{C}-\text{O}$  bond) is energetically favored by  $\sim 12 \text{ kJ mol}^{-1}$  over **t-PA** ( $180^\circ$  dihedral angle).<sup>37,38</sup> The *cis*-to-*trans* interconversion barrier is calculated to be  $\sim 40 \text{ kJ mol}^{-1}$ ,<sup>37,39,40</sup> suggesting a high degree of conformational rigidity, particularly under cryogenic conditions. **c-PA** has been detected across gas, liquid and solid matrices.<sup>29,38,40–42</sup> Notably, the *cis*-to-*trans* isomerization has been reported exclusively through photoinduced processes in confined environments ( $\text{N}_2$  matrix).<sup>38</sup> The dipole moments ( $\mu$ ) of **c-PA** and **t-PA** are 1.59 D and 4.8 D, respectively.<sup>43</sup>

Since PA has pronounced dipole moment and multifunctional hydrogen bonding capabilities, it will be insightful, particularly, for secondary organic aerosol formation and prebiotic chemistry in extraterrestrial environments to explore the binding motifs of PA with molecules like  $\text{H}_2\text{O}$ ,  $\text{H}_2\text{S}$ ,  $\text{CO}_2$ , and  $\text{NH}_3$ , which differ in polarity and bonding behaviour.<sup>44</sup> Here, formation of unconventional HBs involving  $\equiv\text{C}-\text{H}$  and  $\text{C}\equiv\text{C}$  functional groups can be expected in line with previous low temperature studies on monohydrated propyne and acetylene.<sup>16</sup>

In the current work, we present the isolation of the PA monomer and its 1:1 binary complex with  $\text{D}_2\text{O}$  in HNDs. The substantial dipole moment of  $\text{D}_2\text{O}$  ( $\mu = 1.85 \text{ D}$ ) together with PA is expected to influence the geometry and binding orientation of the resulting binary complexes in HNDs. Mass-selective infrared spectra were recorded in the  $\text{C}=\text{O}$  and  $\text{C}\equiv\text{C}$  stretching regions for the PA monomer and the  $\text{PA}\cdot\cdot\text{D}_2\text{O}$  dimer. A controlled formation of 1:1 complexes was achieved through sequential doping of the helium droplets using two spatially separated pickup chambers. Structural assignments were based on the comparison of the experimentally observed IR band positions and intensities with harmonic spectra calculated for the most stable isomers at the MP2 level. Furthermore, the relative stabilities of these identified structures were assessed

using computed interaction energies, offering insights into the preferred binding motifs and the influence of dipole–dipole interaction in molecular aggregation under such confined cryogenic conditions.

## 2. Experiment

### 2.1. Experimental set-up

PA and  $\text{D}_2\text{O}$  were purchased from Sigma-Aldrich and employed without further purification except degassing. The experiments were performed using the infrared helium nanodroplet spectrometer at Ruhr University Bochum.<sup>33,45</sup> This instrument consists of four differentially pumped vacuum chambers – namely, expansion, pick-up, spectroscopy and quadrupole mass spectrometry (QMS) chamber – corresponding to vacuum levels ranging from moderate ( $10^{-5}$  mbar) to ultrahigh vacuum ( $10^{-9}$  mbar), respectively. These given pressure ranges (in mbar) are in the presence of a HND beam. The HNDs are generated *via* a continuous supersonic expansion of highly pressurized (40–50 bar) ultrapure (99.9999%) helium gas through a pre-cooled nozzle of 5  $\mu\text{m}$  diameter into the expansion chamber. A closed-cycle helium cryostat combined with temperature controller maintains the temperature of the nozzle within 13–22 K for droplet production. The droplet size is log-normally distributed and is controlled by varying the backing He pressure and temperature of the nozzle. After expansion, droplets are collimated using a skimmer of 0.5 mm in diameter and introduced into the following pick-up chamber, which consists of two individually pumped and spatially well separated (distance  $\sim 20 \text{ cm}$ ) pick-up cells. They are traversed by the droplet beam *via* 5-mm-diameter openings in the cell walls. Here, dopant molecules are injected into the droplet beam using these pick-up lines, namely pick-up-lines 1 and 2. After passing through the pick-up and the spectroscopy chamber, the droplets are detected using an Extrel quadrupole mass spectrometer (model 5221) in the QMS chamber.

In the present study, expansion conditions were set to  $\sim 45$  bars of He and 19.9 K of nozzle temperature, which led to the formation of droplets containing roughly  $10^4$  He atoms. The droplets were doped by PA using pick-up-line 1 with the pick-up pressure set to  $3.0 \times 10^{-5}$  mbar.  $\text{D}_2\text{O}$  for the generation of the  $\text{PA}\cdot\cdot\text{D}_2\text{O}$  complex is subsequently introduced *via* pick-up-line 2 with the pick-up pressures maintained at  $\sim 3 \times 10^{-5}$  mbar.

To record the vibrational spectra of PA monomer and the  $\text{PA}\cdot\cdot\text{D}_2\text{O}$  dimer, infrared light of a quantum cascade laser from DRS Daylight Solution (model number: MIRCAt-QT-Z-2400) has been employed, where the beam path was continuously purged by  $\text{N}_2$  gas. The laser comprised of four lasing heads encompasses these ranges: 1460–1635, 1620–1860, 1960–2220 and 2290–2520  $\text{cm}^{-1}$ . The laser light overlaps with the droplet beam in an antiparallel configuration. Pure helium droplets are transparent to the IR radiation. However, absorption of the IR photons by the embedded molecules/clusters followed by vibrational relaxation causes evaporation of several hundred helium atoms from the droplet surface (He–He binding energy  $\sim 5 \text{ cm}^{-1}$ ). It leads to



a shrinkage of the droplet ionization cross-section and to a concomitant decrease in the ion current measured by the QMS. Now, recording the dip in the ion current for a specific mass channel ( $m/z$ ) as a function of IR radiation frequency yields the mass-selective vibrational spectrum. The signal is collected using phase-sensitive-detection with a lock-in amplifier.

**Pick-up curve.** For the determination of the cluster size of PA, we have recorded the amplitude of the depletion signal as a function of partial pressures, the so-called pick-up curve, as shown in Fig. S1 in the SI. These pick-up curves follow Poisson statistics<sup>46</sup> and were used to deduce the molecular cluster size corresponding to the observed bands. According to Poisson statistics, the probability of picking up  $k$  dopant molecule(s) is given by the following equation:

$$P_k = [(\sigma\rho L)^k/k!]\exp(-\sigma\rho L)$$

where  $\sigma$  represents the pick-up cross-section of the droplets,  $\rho$  is the number density of the molecules in the pick-up chamber and  $L$  is the length of the pick-up region. Here,  $L$  is a constant for a given experimental setup, and  $\sigma$  can also be considered as a constant for a well-defined droplet size distribution.  $\rho$  is directly proportional to the partial pressure of the dopant in the pick-up chamber.

The IR features originating from the PA  $\cdot\cdot$  D<sub>2</sub>O complex are relatively weak. In addition to pick-up curve measurements (see Fig. S2 in the SI), we plotted pressure-dependent IR spectra for the PA  $\cdot\cdot$  D<sub>2</sub>O complex. In the latter case, the PA pick-up pressure ( $p_{\text{PA}}$ ) was fixed at the monomer value, as determined from Fig. S1, while the D<sub>2</sub>O pick-up pressure ( $p_{\text{D}_2\text{O}}$ ) was systematically varied (see Fig. S3 in the SI). These measurements together with mass spectral analysis (Section 2.3) confirm the cluster size of the PA  $\cdot\cdot$  D<sub>2</sub>O complex.

## 2.2. Computation

Geometry optimization and harmonic vibrational frequency calculations were performed for the PA monomer as well as its 1:1 complexes with D<sub>2</sub>O using MP2/aug-cc-pVDZ and B3LYP-D3/cc-pVTZ methods.<sup>47,48</sup> From our earlier observations,<sup>33</sup> we found that the helium droplet experimental spectra of organic acids and their complexes are well reproduced by harmonic IR spectra calculated at the MP2/aug-cc-pVDZ level. Therefore, these MP2-computed frequencies are employed to assist in the structural assignment of the experimental spectra and to derive zero-point-energy (ZPE) corrected relative energies ( $\Delta E_0$ ). A scaling factor of 1.00 (no scaling) determined by comparing the computed C=O and C≡C stretching frequencies of the PA monomer with their corresponding observed values inside HNDs is used. The BSSE-corrected [BSSE: basis set superposition error] interaction energies ( $D_0$ ) for 1:1 PA  $\cdot\cdot$  D<sub>2</sub>O complexes are also calculated using the counterpoise method, where the energies of the complexes are calculated alongside the energies of the individual monomers, both with the same basis set.<sup>49,50</sup> Note that relative stabilities of the isomers are discussed based on MP2-obtained  $\Delta E_0$  and  $D_0$  values. The geometry optimization at the

DFT level were performed additionally to validate and verify real minima obtained at the MP2 level. Note that an empirical dispersion correction (D3) was included in the DFT geometry optimizations to account for dispersion interactions.<sup>51</sup> All computations are performed using Gaussian 16 software.<sup>52</sup> Optimized geometry and cartesian coordinates of all relevant structures are provided in Table S1a and b in the SI.

## 2.3. Structure nomenclature scheme

The labelling of the two monomer structures of PA as *cis*-PA (*c*-PA) and *trans*-PA (*t*-PA) is based on *cis* and *trans* orientations of C=O and O-H groups along the C-O single bond axis.<sup>38</sup> Structures corresponding to the 1:1 complex of PA with D<sub>2</sub>O are systematically labelled following the scheme *c/t*-PAm-*n*, where *m* denotes the interacting molecule with PA (*m* = *w* for D<sub>2</sub>O). The integer *n* is assigned in the ascending order of computed relative energies ( $\Delta E_0$ ) of the isomers where *n* = 1 is for the global minimum. Water molecules are labelled according to their role as HB donors (D) or acceptors (A). For example, a D<sub>2</sub>O molecule simultaneously acting as a donor and an acceptor is designated as AD-D<sub>2</sub>O.

## 3. Results and discussion

### 3.1. Mass spectra

Fig. 1 shows a comparison of the mass spectra of the pure helium droplet beam (trace a, black), doped with PA at  $p_{\text{PA}} = 3.0 \times 10^{-5}$  mbar (trace b, red), droplets doped with D<sub>2</sub>O at  $p_{\text{D}_2\text{O}} = 3.0 \times 10^{-5}$  mbar (trace c, green), and droplets doped subsequently with PA and D<sub>2</sub>O from pick-up lines 1 and 2 both set at  $p_{\text{PA}}$  and  $p_{\text{D}_2\text{O}} = 3.0 \times 10^{-5}$  mbar (trace d, blue). The peaks at a multiple of  $m/z = 4$  amu correspond to (<sup>4</sup>He)<sub>*n*</sub><sup>+</sup> fragments

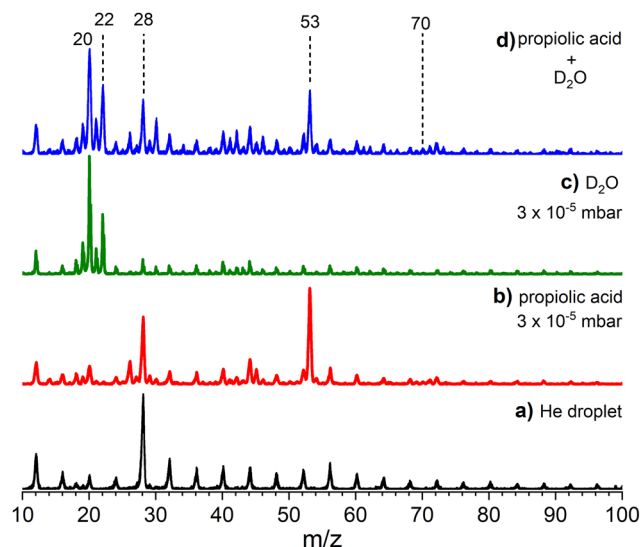


Fig. 1 Mass spectra of droplet beam of (a) pure helium and doped droplets with (b) propionic acid (PA) at a pick-up pressure of  $3.0 \times 10^{-5}$  mbar, (c) D<sub>2</sub>O at a pick-up pressure of  $3.0 \times 10^{-5}$  mbar, and (d) PA and D<sub>2</sub>O both set to the pick-up pressure of  $3.0 \times 10^{-5}$  mbar from two different pick-up lines.



(see trace 1a); the very small peak at  $m/z = 18$ , is due to residual water vapor in the instrument (see trace 1a). As the intensity of the  $m/z = 18$  peak is five times smaller than that of  $m/z = 16$  corresponding to the  $(^4\text{He})_4^+$ , it has no impact on the spectral measurements. The peak at  $m/z = 28$ , attributed to the  $(^4\text{He})_7^+$  and trapped  $\text{N}_2$ , is relatively strong. Note, the absence of a 3 : 1 intensity ratio between the  $m/z = 28$  and  $m/z = 32$  peaks, corresponding to the natural abundances of  $\text{N}_2$  and  $\text{O}_2$ , respectively, rules out any contribution from atmospheric sources. The mass spectrum of the droplets doped at  $p_{\text{PA}} = 3.0 \times 10^{-5}$  mbar yields additional peaks at  $m/z = 25, 28, 45, 53$  and  $70$  with  $m/z = 53$  being the dominant one (see trace 1b). Here,  $m/z = 70$  corresponds to the PA molecular ion  $(\text{HC}\equiv\text{C}-\text{COOH})^+$ , while the mass fragments at  $m/z = 25, 28, 45, 53$  represent the species  $(\text{C}_2\text{H})^+, (\text{CO})^+, (\text{COOH})^+, (\text{HC}\equiv\text{CCO})^+$ , respectively.  $\text{D}_2\text{O}$  doping at  $p_{\text{D}_2\text{O}} = 3.0 \times 10^{-5}$  mbar yielded the most prominent molecular mass peak  $(\text{D}_2\text{O})^+$  at  $m/z = 20$  as well as a smaller peak at  $m/z = 22$   $(\text{D}_3\text{O})^+$  (trace 1c). This mass spectral pattern indicates the condition which corresponds to the single  $\text{D}_2\text{O}$  molecule doping. Trace 1d shows the mass spectrum obtained after sequential doping of helium droplets with PA and  $\text{D}_2\text{O}$ , both at the pick-up pressure of  $3 \times 10^{-5}$  mbar.

### 3.2. Experimental infrared spectra

**PA and PA  $\cdot$   $\text{D}_2\text{O}$ .** In Fig. 2 and Fig. 3, we display mass-selective [ $m/z = 53, (\text{HC}\equiv\text{C}-\text{C}=\text{O})^+$ ] IR spectra of PA and the PA  $\cdot$   $\text{D}_2\text{O}$  complex, trapped inside HNDs, in the C=O and the C $\equiv$ C stretching frequency range, respectively. The IR traces of PA recorded at the  $p_{\text{PA}} = 3 \times 10^{-5}$  mbar are shown in black (Fig. 2a and 3a). The red traces (Fig. 2b and 3b) show the IR spectra of the PA  $\cdot$   $\text{D}_2\text{O}$  complex formed *via* sequential pickup of PA and  $\text{D}_2\text{O}$  in HNDs, with both pick-up pressures maintained at  $3 \times 10^{-5}$  mbar.

The IR spectrum of PA in the C=O stretching range is dominated by the strong feature located at  $1762.5 \text{ cm}^{-1}$ , designated as  $A_1$  (see trace 2a, black). In addition, two weak bands ( $\sim 15$  times less intense than  $A_1$ ) are observed within  $3 \text{ cm}^{-1}$ . These absorptions are marked with asterisks in trace 2a.



Fig. 2 Mass-selected ( $m/z = 53$ ) IR spectra in the C=O stretching region of (a) the PA monomer ( $p_{\text{PA}} = 3 \times 10^{-5}$  mbar) and (b) the PA  $\cdot$   $\text{D}_2\text{O}$  complex *via* a sequential pickup of PA ( $p_{\text{PA}} = 3 \times 10^{-5}$  mbar) and  $\text{D}_2\text{O}$  ( $p_{\text{D}_2\text{O}} = 3 \times 10^{-5}$  mbar) in helium nanodroplets. IR absorption bands of PA and the PA  $\cdot$   $\text{D}_2\text{O}$  complex are denoted by  $A_1$  and  $a_1$ – $a_3$ , respectively. In the inset, we plot the range  $1725$ – $1750 \text{ cm}^{-1}$  displaying the bands  $a_2$  and  $a_3$ . The substantially weak features in trace 2a are marked with asterisks.



Fig. 3 Mass-selected ( $m/z = 53$ ) IR spectra in the C $\equiv$ C stretching region of (a) PA monomer ( $p_{\text{PA}} = 3 \times 10^{-5}$  mbar) and (b) PA  $\cdot$   $\text{D}_2\text{O}$  complex *via* a sequential pickup of PA ( $p_{\text{PA}} = 3 \times 10^{-5}$  mbar) and  $\text{D}_2\text{O}$  ( $p_{\text{D}_2\text{O}} = 3 \times 10^{-5}$  mbar) in helium nanodroplets. Traces a and b are normalized to the intensity of the  $A_3$  band. The strongest IR absorption of the monomer is denoted as  $A_3$  and the shoulder to  $A_2$ . The bands marked with  $a_4$  and  $a_5$  correspond to the PA  $\cdot$   $\text{D}_2\text{O}$  complex.

In the C $\equiv$ C stretching region (Fig. 3a), a moderately intense feature at  $2142.6 \text{ cm}^{-1}$  ( $A_3$ ) is detected with a shoulder at  $2141.6 \text{ cm}^{-1}$  ( $A_2$ ). Pick-up curve analysis indicates that the dominant features at  $1762.5$  and  $2142.6 \text{ cm}^{-1}$  are due to the PA monomer (see Fig. S1).

Previous studies in solid matrices ( $\text{N}_2$ , Ar and Ne) identified the C=O and C $\equiv$ C stretching vibrations of the *cis*-PA (**c-PA**) conformer at around  $1755$  and  $2140 \text{ cm}^{-1}$ , respectively.<sup>38,43</sup> In gas-phase FTIR measurements, two broad features centered around  $1745$  and  $2137 \text{ cm}^{-1}$  are attributed to **c-PA**.<sup>42</sup> Therefore, the observed bands  $A_1$  and  $A_3$  in HNDs can be assigned to the C=O and C $\equiv$ C stretching modes of the **c-PA** conformer, respectively (see Table 1). In line with the present helium droplet study, matrix isolation measurements also reported weak features adjacent to the dominant IR bands ( $A_1$  and  $A_3$ ). These additional bands marked by asterisks in trace 2a and the  $A_2$  peak in trace 3a could be due to anharmonic effects—such as combination bands, overtones, or Fermi resonances (*vide infra*).

Now, formation of the PA  $\cdot$   $\text{D}_2\text{O}$  dimers inside the HNDs results in the emergence of three new IR absorption bands, located at  $1758.5 \text{ cm}^{-1}$  ( $a_1$ ),  $1743.3 \text{ cm}^{-1}$  ( $a_2$ ), and  $1729.5 \text{ cm}^{-1}$  ( $a_3$ ), in the C=O stretching region (summarized in Table 1). The  $a_1$  feature overlaps slightly with a tiny band from the PA monomer. Hence, this peak is delineated by a dashed line to aid visual identification (see trace a *vs.* trace b, Fig. 2). A magnified view of the  $1725$ – $1750 \text{ cm}^{-1}$  range (inset) provides a clearer view of  $a_3$  along with its relative intensity compared to  $a_2$  (Fig. 2). It is important to note that the narrowest band,  $a_1$  (FWHM =  $0.5 \text{ cm}^{-1}$ ), exhibits only a redshift of  $4 \text{ cm}^{-1}$  relative to the C=O stretch of the PA monomer ( $A_1$ ,  $1762.5 \text{ cm}^{-1}$ ). However, a substantial bathochromic shift of  $\sim 34 \text{ cm}^{-1}$  is observed for the broadest band,  $a_3$  (FWHM =  $2.0 \text{ cm}^{-1}$ ). The feature  $a_2$  displays a redshift of approximately  $19 \text{ cm}^{-1}$  with FWHM  $\sim 1.0 \text{ cm}^{-1}$ . This trend reveals an inverse correlation between redshift and spectral linewidth (FWHM) across the three bands suggesting that they are likely originating from structural motifs of varying hydrogen bonding strengths.

The two new absorptions at  $2134.6 \text{ cm}^{-1}$  ( $a_4$ ) and  $2141.7 \text{ cm}^{-1}$  ( $a_5$ ) in the C $\equiv$ C stretching region are assigned to the



**Table 1** Comparison of observed IR band positions of the propiolic acid (PA) monomer and 1:1 PA $\cdots$ D<sub>2</sub>O complexes isolated in helium nanodroplets with MP2/aug-cc-pVDZ computed harmonic frequencies. Very weak absorption features from PA monomer are denoted by asterisks, see trace 2a. Previously reported values of the PA monomer trapped in N<sub>2</sub>, neon (Ne), argon (Ar) matrices and in the gas-phase are included for reference. The MP2-calculated transitions from Section 3.3 were employed to assist in the vibrational assignments

Species	Observed transition (cm <sup>-1</sup> )				Gas-phase <sup>d</sup>	Calculated (cm <sup>-1</sup> ) <sup>e</sup>	Vibrational assignments
	He droplet	N <sub>2</sub> <sup>a</sup>	Ne <sup>b</sup>	Ar <sup>c</sup>			
PA	1759.1(*)		1756				
	1761.1(*)						
	1762.5 (A <sub>1</sub> )	1754	1759	1754	1745	1762	C=O str. ( $\nu_3$ )
	2141.6 (A <sub>2</sub> )		2136				
	2142.6 (A <sub>3</sub> )	2140	2140	2137	2137	2140	C $\equiv$ C str. ( $\nu_4$ )
PA $\cdots$ D <sub>2</sub> O	1758.5 (a <sub>1</sub> )					1759	C=O str. ( <b>c-PAw-3</b> )
	1743.3 (a <sub>2</sub> )					1745	C=O str. ( <b>c-PAw-2</b> )
	1729.5 (a <sub>3</sub> )					1731	C=O str. ( <b>c-PAw-1</b> )
	2134.6 (a <sub>4</sub> )					2132	C $\equiv$ C str. ( <b>c-PAw-3</b> )
	2141.7 (a <sub>5</sub> )					2143	C $\equiv$ C str. ( <b>c-PAw-2</b> )

<sup>a</sup> Observed in the N<sub>2</sub> matrix at 12 K.<sup>38</sup> <sup>b</sup> Observed in the Ne matrix at  $\sim$ 10 K.<sup>43</sup> <sup>c</sup> Observed in the Ar matrix at 9 K.<sup>40</sup> <sup>d</sup> FTIR measurements in the gas-phase at room temperature.<sup>42</sup> <sup>e</sup> MP2/aug-cc-pVDZ computed IR band frequencies in the current study.

PA $\cdots$ D<sub>2</sub>O complex (see trace 3b vs. trace 3a). Note that peak a<sub>5</sub> overlaps significantly with the features from the PA monomer. However, a normalization of traces a and b of Fig. 3 to the intensity of peak A<sub>3</sub> supports the existence of the band a<sub>5</sub>. The a<sub>4</sub> feature exhibits a red shift of approximately 8 cm<sup>-1</sup> relative to the corresponding A<sub>3</sub> band of the PA monomer, whereas a<sub>5</sub> shows a shift of less than 1 cm<sup>-1</sup> (Table 1). This contrasting behavior suggests distinct binding motifs: for a<sub>4</sub>, the C $\equiv$ C unit is likely directly involved in the interaction with D<sub>2</sub>O, while in the case of a<sub>5</sub>, the C $\equiv$ C moiety remains largely unaffected, indicating an indirect or more distant binding configuration.

We have measured pick up curves (see Figure S2 in the SI) and plotted pressure-dependent IR spectra (Figure S3) to confirm the assignment of a<sub>1</sub>, a<sub>2</sub>, a<sub>3</sub> and a<sub>4</sub> to the 1:1 PA $\cdots$ D<sub>2</sub>O dimer. A similar analysis for band a<sub>5</sub> is not possible due to the significant overlap with monomer features.

**PA $\cdots$ H<sub>2</sub>O.** To account for isotopic effects, IR spectra of the PA $\cdots$ H<sub>2</sub>O complex were recorded in both the C=O and C $\equiv$ C stretching regions (Fig. S4 and S5, SI). In monohydrated systems, the C=O stretching frequency is generally weakly affected by isotopic (H<sub>2</sub>O/D<sub>2</sub>O) substitution. Consistent with this, bands a<sub>2</sub> and a<sub>5</sub> exhibit only minor shifts (within  $\pm$ 0.5 cm<sup>-1</sup>), while bands a<sub>3</sub> and a<sub>4</sub> show no detectable change compared to the PA $\cdots$ D<sub>2</sub>O complex. Based on the observation, we propose that group (a<sub>1</sub>, a<sub>4</sub>) and (a<sub>2</sub>, a<sub>5</sub>) are associated with two different isomers. This spectral grouping is verified later in Section 3.3.

### 3.3 Structural assignments

Geometry optimization and harmonic frequency calculation for the plausible isomers of the PA monomer and the 1:1 complex of PA $\cdots$ D<sub>2</sub>O were carried out to aid structural assignment of the experimental spectra. The lowest-energy structures of the PA monomer and PA $\cdots$ D<sub>2</sub>O dimer according to their relative energies ( $\Delta E_0$ ) obtained at MP2/aug-cc-pVDZ level are plotted in the left and right panels of Fig. 4, respectively. Additionally, Table 2 and Table S3 in the SI provide  $\Delta E_0$  and structural parameters obtained both at MP2 and DFT levels. BSSE-

corrected interaction energies ( $D_0$ ) in Table 2 are obtained at the MP2 level.

**3.3.1. PA monomer.** As mentioned earlier, **c-PA** is reported to be the global minimum whereas **t-PA** is 12–16 kJ mol<sup>-1</sup> higher in energy.<sup>31</sup> In accordance with the previous findings, our current MP2 and DFT calculations confirm **c-PA** as the global minimum, with **t-PA** residing approximately 12 kJ mol<sup>-1</sup> above (Table 2). The optimized structures and corresponding dipole moment vectors (arrows in cyan) of these conformers are presented in Fig. 4 (left panel).

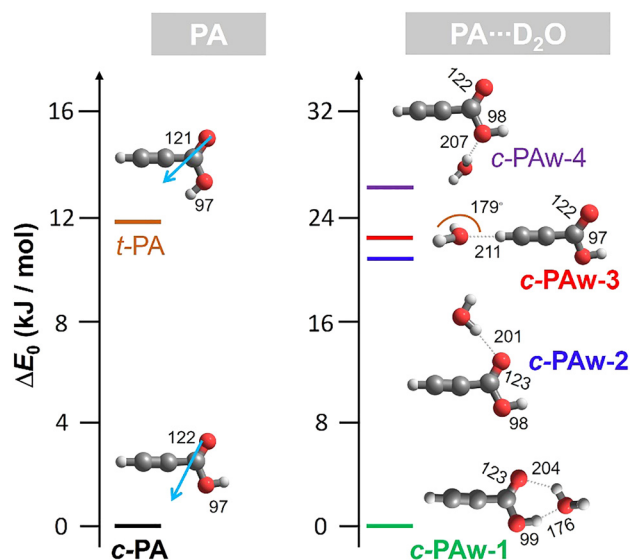


**Fig. 4** ZPE-corrected relative energies  $\Delta E_0$  obtained at the MP2/aug-cc-pVDZ level for the lowest energy structures of the PA monomer and the **c-PA** $\cdots$ D<sub>2</sub>O dimer are presented in the left and right panels, respectively, with color coded bars. The nomenclature scheme is elaborated in Section 3.2. The name of the species identified in helium droplets are in bold. Bond distances and angle are in picometers (pm) and degrees ( $^\circ$ ), respectively. The orientation of dipole moments for PA conformers are shown by arrows. Additional lowest energy structures for 1:1 complexes can be found in Table S1 in the SI.



**Table 2** ZPE-corrected relative energies ( $\Delta E_0$ ) for the lowest energy isomers of the propiolic acid (PA) monomer and the PA $\cdots$ D<sub>2</sub>O dimer calculated at MP2 and DFT levels. The hydrogen bond distances ( $r_{\text{HB}}$ ) and BSSE-corrected interaction energies ( $D_0$ ) at the MP2 level are in picometers and kJ mol<sup>-1</sup>, respectively

Species	Isomers	MP2/aug-cc-pVDZ				B3LYP-D3/cc-pVTZ	
		Symm.	$\Delta E_0$ (kJ mol <sup>-1</sup> )	$r_{\text{HB}}$ (pm)	$D_0$ (kJ mol <sup>-1</sup> )	$\Delta E_0$ (kJ mol <sup>-1</sup> )	$r_{\text{HB}}$ (pm)
PA	<b>c-PA</b>	$C_s$	0.0			0.0	
	<b>t-PA</b>	$C_s$	11.7			11.5	
PA $\cdots$ D <sub>2</sub> O	<b>c-PAw-1</b>	$C_1$	0.0	176 & 204	32.6	0.0	173 & 199
	<b>c-PAw-2</b>	$C_s$	21.0	201	12.4	29.1	202
	<b>c-PAw-3</b>	$C_s$	22.9	211	11.3	29.0	209
	<b>c-PAw-4</b>	$C_1$	26.5	207	6.0	34.5	214

The vibrational spectra of PA, recorded in both the solid state (Ne matrix) and gas phase (vapor at room temperature), display distinct bands corresponding to the C=O and C $\equiv$ C stretching modes. Precisely, the C=O stretching vibration appears at 1759 cm<sup>-1</sup> in the Ne matrix and shifts to 1745 cm<sup>-1</sup> in the vapor phase. The C $\equiv$ C stretching band is observed at 2140 cm<sup>-1</sup> in the solid neon and at 2137 cm<sup>-1</sup> in the vapor phase (see Table 1). Ar matrix data are also in accordance, reporting C=O and C $\equiv$ C stretching vibrations at 1754 and 2137 cm<sup>-1</sup>, respectively.<sup>40</sup> In addition, a recent matrix-isolation study in solid N<sub>2</sub> reported the C=O stretch of **c-PA** at  $\sim$ 1754 cm<sup>-1</sup> and of **t-PA** at  $\sim$ 1780 cm<sup>-1</sup>. In the N<sub>2</sub>-matrix, the higher energy **t-PA** conformer was selectively populated *via* UV irradiation.<sup>38</sup>

We compare the IR spectra of the PA monomer in helium nanodroplets recorded at the C=O and C $\equiv$ C stretching regions with the MP2-calculated spectra of its possible conformers (Fig. 5). The observed bands at 1762.5 cm<sup>-1</sup> (A<sub>1</sub>) and 2142.6 cm<sup>-1</sup> (A<sub>3</sub>) are in excellent agreement with the computed transitions of **c-PA** (trace 5a vs. 5b). So, the *cis* conformer of the PA monomer has been exclusively isolated inside the He droplet which is consistent with previous gas- and solid-phase findings.

Now, to address the assignment of weakly intense features (marked with asterisk and A<sub>2</sub>, Fig. 5), we performed

anharmonic calculations. Because the positions and intensities of the IR bands originated from anharmonicity are highly sensitive to the ground-state structure, we computed the anharmonic IR spectra of **c-PA** at multiple levels of theory, each producing noticeable variations (see the bottom trace of Fig. S6 in the SI). The anharmonic spectrum computed at the VPT2/MP2/aug-cc-pVDZ level (see Fig. S6 in the SI) does not accurately reproduce the weak experimental features, preventing an unambiguous mode assignment. However, tentatively the tiny feature A<sub>2</sub> can be attributed to a combination band involving the C–C–OH stretching and O–H in-plane bending vibrations. Since these bands are extremely weak in intensity compared to the dominant feature A<sub>1</sub> and A<sub>3</sub>, we refrain from making further vibrational assignments for them.

**3.3.2. PA $\cdots$ D<sub>2</sub>O dimer.** PA comprised of carboxylic (–COOH) and acetylic (HC $\equiv$ C–) functional groups provides multiple potential hydrogen bonding sites for D<sub>2</sub>O. As **c-PA** has been exclusively identified as the isolated species in helium droplet (see Section 3.3.1), we focused only on complexes of **c-PA** with D<sub>2</sub>O. A comprehensive potential energy surface scan was performed to identify the lowest-energy geometries of the **c-PA** $\cdots$ D<sub>2</sub>O complex. Four distinct HB sites were found: (i) AD-D<sub>2</sub>O doubly hydrogen bonded to COOH group (**c-PAw-1**), (ii) D-D<sub>2</sub>O singly hydrogen bonded to carbonyl oxygen atom (**c-PAw-2**), (iii) A-D<sub>2</sub>O singly hydrogen bonded to H–C $\equiv$ C moiety (**c-PAw-3**), and (iv) D-D<sub>2</sub>O singly hydrogen bonded to hydroxyl oxygen atom (**c-PAw-4**). These structures are presented in Fig. 4 (left panel).

Briefly, the global minimum **c-PAw-1** is the lowest symmetric ( $C_1$ ) structure and characterized by a six-membered ring formation where D<sub>2</sub>O and PA moieties simultaneously serve as HB donors and acceptors. The HB length in which the water molecule functions as the acceptor, *i.e.*, –O–H $\cdots$ OD<sub>2</sub>, is predicted to be approximately 15% shorter than the one where D<sub>2</sub>O serves as the donor, *i.e.*, –C=O $\cdots$ DOD (see Table 2 and Fig. 4). The second-lowest energy structure, **c-PAw-2**, lying 21 kJ mol<sup>-1</sup> above **c-PAw-1**, adopts  $C_s$  symmetry. The corresponding HB length is calculated to be 201 pm, closely matching the weaker HB length in **c-PAw-1** (204 pm). Isomer **c-PAw-3** ( $C_s$  symm.) found 22.9 kJ mol<sup>-1</sup> above the global minimum exhibits a so-called non-classical HB. In this case, the D<sub>2</sub>O molecule acts as a HB acceptor, while the acetylenic hydrogen ( $\equiv$ C–H) is the HB donor. The resulting HB distance is comparatively longer, 211 pm. The  $C_2$  principal axis of D<sub>2</sub>O (aligned with its dipole



**Fig. 5** Comparison of (a) the experimental infrared spectrum of the propiolic acid (PA) with the MP2/aug-cc-pVDZ calculated harmonic IR spectra for the two lowest energy structures (b) **c-PA** and (c) **t-PA**. ZPE-corrected relative energies ( $\Delta E_0$ ) in parenthesis are in kJ mol<sup>-1</sup>.



moment vector) is nearly colinear with the C≡C–H axis of PA, forming an angle of  $\sim 179^\circ$  (Fig. 4). The 4th lowest energy isomer **c-PAw-4** ( $\Delta E_0 = +26.5$  kJ mol $^{-1}$ ,  $C_1$  symm.) exhibits a HB of 207 pm distance. Note, a similar trend in  $\Delta E_0$  value is also found at DFT level as listed in Table 2.

Nevertheless, stability of these binding motifs is further substantiated by calculating interaction energies ( $D_0$ ) for each isomer at the MP2 level. The  $D_0$  value for **c-PAw-1** is 33 kJ mol $^{-1}$ , which is more than twice as stabilizing as that of the **c-PAw-2** (12 kJ mol $^{-1}$ ) as listed in Table 2. This substantial  $D_0$  value for **c-PAw-1** directly reflects the cooperative effect of its dual hydrogen-bonded motif. Notably,  $D_0$  values for **c-PAw-2** and **c-PAw-3** are nearly similar, whereas **c-PAw-4** exhibits a marked difference (see Table 2).

For completeness, geometry optimization seeking for lowest energy isomers of **t-PA**· $D_2O$  complex is also performed. The structures and their corresponding  $\Delta E_0$  values relative to the global minimum **c-PAw-1** are provided in Table S1 in the SI.

The IR spectrum of the **c-PA**· $D_2O$  1:1 complex (trace a, Fig. 6) displays five prominent vibrational bands:  $a_1$  (1758.5 cm $^{-1}$ ),  $a_2$  (1743.3 cm $^{-1}$ ),  $a_3$  (1729.5 cm $^{-1}$ ),  $a_4$  (2134.6 cm $^{-1}$ ) and  $a_5$  (2141.7 cm $^{-1}$ ). According to the analysis at Section 3.2 above, ( $a_1$ ,  $a_4$ ) and ( $a_2$ ,  $a_5$ ) are attributed to two different isomers. Anyways, MP2-computed harmonic vibrational frequencies in

the C=O and C≡C stretching regions for all four isomers, **c-PAw-1** to **c-PAw-4**, are compared with the experimental IR spectrum recorded in helium droplet to carry out structural assignment (see Fig. 6). As the water binding motifs in each of these four lowest energy isomers are distinctive, characteristic differences in their predicted IR spectra are evident. Calculated spectra for **c-PAw-3**, **c-PAw-2**, **c-PAw-1**, and **c-PAw-4**, are plotted in trace b (red), c (blue), d (green), and e (violet) of Fig. 6, respectively. The experimental bands  $a_1$  (1758.5 cm $^{-1}$ ) and  $a_4$  (2134.6 cm $^{-1}$ ), highlighted in red, are closely reproduced by the spectrum computed for the isomer **c-PAw-3**. The predicted frequencies for the C=O and C≡C stretching modes in **c-PAw-3** are 1759 cm $^{-1}$  and 2132 cm $^{-1}$ , respectively—both within  $\Delta\nu = \pm 2$  cm $^{-1}$  of the experimental values, indicating good agreement between theory and experiment (traces a vs. b). Furthermore, bands  $a_2$  (1743.3 cm $^{-1}$ ) and  $a_5$  (2141.7 cm $^{-1}$ ), displayed in blue, are reproduced by the IR transitions computed for the species **c-PAw-2**. Precisely, the predicted frequencies corresponding to the C=O and C≡C stretching modes for **c-PAw-2** are 1745 cm $^{-1}$  and 2153 cm $^{-1}$ , respectively—both within  $\Delta\nu = \pm 2$  cm $^{-1}$  of the experimental values, establishing also satisfactory agreement between theory and experiment (traces a vs. c).

The broadest peak  $a_3$  (1729.5 cm $^{-1}$ , green) lies near to the computed C=O stretching mode of the global minimum isomer **c-PAw-1** at 1732 cm $^{-1}$  (trace a vs. trace d). The frequency deviation is within  $\Delta\nu = \pm 3$  cm $^{-1}$ , further supporting this structural assignments. However, the associated C≡C stretching bands predicted for the **c-PAw-1** was not observed experimentally. This is consistent with computational predictions, which indicate that the C≡C stretching modes exhibit infrared intensities approximately one-fifth of those associated with the C=O stretching vibrations. Besides, the feature is predicted to be in overlap with stronger absorptions of the PA monomer. In summary, we have identified the following structures: **c-PAw-3**, **c-PAw-2** and **c-PAw-1** inside HNDs based on the comparison between experiment and theory. The vibrational assignments are listed in Table 1.

### 3.4. Discussion

The three isomers, **c-PAw-1**, **c-PAw-2**, and **c-PAw-3**, observed upon PA· $D_2O$  dimerization within HNDs, exhibit a broad range of relative stabilities and distinct hydrogen-bonding motifs (classical and non-classical) involving both C=O and C≡C moieties. The stabilization of local minimum structures (**c-PAw-2** and **c-PAw-3**) is likely governed by the kinetic trapping at ultra-low temperature (0.4 K) inside HNDs.

Low-temperature spectroscopic measurements combined with computational study on the complexes of acetylene (HC≡CH) and propyne (CH<sub>3</sub>-C≡CH) with a single water molecule has previously revealed distinct binding motifs where non-classical HB generation is dominating.<sup>16</sup> Particularly, the presence of  $\alpha$ -hydrogens on the methyl group adjacent to the C≡C bond in CH<sub>3</sub>-C≡CH enables the formation of a five-membered ring involving the C≡C bond, methyl C–H and the AD-H<sub>2</sub>O in  $\equiv C \cdots H(H)O \cdots HC-$  fashion. Contrarily, the



Fig. 6 Comparison of (a) the experimental IR spectrum of the **c-PA**· $D_2O$  1:1 complex (peaks  $a_1$ ,  $a_2$ ,  $a_3$ ,  $a_4$  and  $a_5$ ) with the MP2/aug-cc-pVDZ calculated harmonic IR spectra for the lowest energy structures (b) **c-PAw-3**, (c) **c-PAw-2**, (d) **c-PAw-1** and (e) **c-PAw-4**. Structural assignments are denoted by color coding.  $\Delta E_0$  (kJ mol $^{-1}$ ) are in parenthesis. Peaks belonging to the **c-PA** monomer in trace a are marked with asterisks. The peak position of the overlapped feature  $a_5$  is shown by an arrow in blue. Dashed lines are used as a guide to the eye for the  $>2000$  cm $^{-1}$  region.



**Table 3** HB motifs for the 1 : 1 complex of **c-PA** ( $\text{HC} \equiv \text{CCOOH}$ ) with  $\text{D}_2\text{O}$  stabilized inside helium nanodroplets as marked with  $\checkmark$ . Calculated interaction energies ( $D_0$ ) are in  $\text{kJ mol}^{-1}$ . The dipole moment ( $\mu$ ) vector of each individual molecular units (*i.e.* PA and  $\text{D}_2\text{O}$ ) are shown by arrows. The  $\mu$  values for **c-PA** and  $\text{D}_2\text{O}$  are 1.59 and 1.85 D, respectively

Hydrogen Bond Motifs	HC $\equiv$ CCOOH + D <sub>2</sub> O	
	He droplet	$D_0$ ( $\text{kJ mol}^{-1}$ )
<b>c-PAw-3</b> 	$\checkmark$	11
<b>c-PAw-2</b> 	$\checkmark$	12
<b>c-PAw-1</b> 	$\checkmark$	32

$\text{HC} \equiv \text{CH}$  molecule forms a linear complex ( $\equiv \text{C}-\text{H} \cdots \text{OH}_2$ ) where the water molecule acts as  $\text{A}-\text{H}_2\text{O}$ . The present study disclosed a similar binding pattern in the isomer **c-PAw-3**. So, the absence of  $\alpha$ -hydrogens adjacent to the  $\text{C} \equiv \text{C}$  group in PA facilitates the  $\equiv \text{C}-\text{H} \cdots \text{OD}_2$  binding. However,  $\text{D}_2\text{O}$  in **c-PAw-2** and **c-PAw-1** forms HB involving the carboxylic acid group only. These findings highlight the diverse hydrogen bonding topologies accessible to PA under superfluid conditions, which is in line with earlier helium droplet experiments on prototypical systems, *i.e.* monohydrated propargyl alcohol ( $\text{H}_2\text{O} \cdots \text{HC} \equiv \text{C}-\text{CH}_2\text{OH}$ ).<sup>36</sup>  $\text{HC} \equiv \text{C}-\text{CH}_2\text{OH}$  has a dipole moment of 1.53 D and the complexation proceeded *via* a dipole-steering mechanism leading to the formation of two local minimum structures stabilized by  $\equiv \text{C}-\text{H} \cdots \text{OD}_2$  and  $-\text{CH}_2\text{O}(\text{H}) \cdots \text{DOD}$  HB formation. In helium droplets, the typical time interval between successive pickup events is on the order of microseconds, while the cooling of molecules inside the droplets occurs within nanoseconds.<sup>35</sup> Consequently, each molecular unit picked up from different pickup events becomes fully thermalized to the droplet temperature ( $\sim 0.4$  K) before aggregation. At this ultralow temperature, thermal energy is negligible, and molecular aggregation is initially guided by long-range electrostatic forces, *i.e.* dipole-dipole interactions, which have  $1/R^3$  distance ( $R$ ) dependence. Considering PA (1.59 D) and  $\text{D}_2\text{O}$  (1.85 D) with substantial permanent dipole moments, dipole-dipole steering pathway plays a fundamental role in their aggregation process.

Now, the relative orientations of the dipole moment vectors of individual molecules in the complexes stabilized inside the helium droplets, **c-PAw-3**, **c-PAw-2**, and **c-PAw-1**, are found not to be head-to-tail but rather appear to be quite random (see Table 3). This observation can be explained by considering a two-step mechanism of dimer formation: (i) initial long-range approach governed by dipole-dipole realignment, (ii) subsequent short-range stabilization driven by the most feasible hydrogen bonding interactions during the time of contact. This successive pathway leading to the formation of local minimum structure for pyruvic and formic acid dimers in HNDs are already reported.<sup>21,31,33,53</sup>

It is also important to emphasize that kinetic trapping to local minima at  $\sim 0.4$  K is possible, as the system lacks

sufficient thermal energy to overcome even modest interconversion barriers. This phenomenon accounts for the significant experimental populations observed for the local minimum structures **c-PAw-3** ( $\Delta E_0 = +22.9 \text{ kJ mol}^{-1}$ ) and **c-PAw-2** ( $\Delta E_0 = +21.0 \text{ kJ mol}^{-1}$ ), despite the greater thermodynamic stability of the global minimum structure **c-PAw-1**. Notably, the order of interaction energies ( $D_0$ ) among these isomers does not correlate with their observed abundances, further supporting the role of kinetic and not thermodynamic control under ultracold conditions (see Tables 2 and 3). The computed barrier for interconversion between **c-PAw-2** and **c-PAw-1**, involving reorientation of the water molecule, is approximately  $2 \text{ kJ mol}^{-1}$  (Fig. S7, left panel in the SI). While relatively low on an absolute energy scale, this barrier remains prohibitively high at 0.4 K. A relaxed scan along the angle between the  $\text{C}=\text{O}$  group of the acid and the O atom of the water molecule was performed, which resulted the transition from **c-PAw-1** to a structure close to **c-PAw-4**. The pathway was found to be barrierless (see Fig. S7, right panel). Since we have already confirmed **c-PAw-4** as a real minimum, this indicates that a very low barrier exists from **c-PAw-4** to **c-PAw-1**. However, this barrier is small enough to be overcome by the energy released at time of interaction between PA and  $\text{D}_2\text{O}$ , which rationalizes why **c-PAw-4** is not observed experimentally. A similar scenario was observed in acetylene-furan trimer formation inside helium droplet.<sup>54</sup>

So, the 1 : 1 PA  $\cdots$   $\text{D}_2\text{O}$  dimer highlight the crucial interplay between long-range dipole-dipole forces and shorter-range interactions in guiding aggregation pathways at ultracold temperatures. The vibrational features of these kinetically trapped higher-energy isomers in the PA  $\cdots$   $\text{D}_2\text{O}$  system may serve as distinctive spectral markers for identifying similar binding motifs in both terrestrial and extraterrestrial environments.

## 4. Conclusions

We report the characterization of the propiolic acid (PA) monomer and its binary complexes with  $\text{D}_2\text{O}$  in helium droplets using mass-selective infrared spectroscopy in the  $\text{C}=\text{O}$  and  $\text{C} \equiv \text{C}$  stretching regions. Five IR absorption bands of 1 : 1 PA  $\cdots$   $\text{D}_2\text{O}$  species reveal the stabilization of three isomers, with  $\text{D}_2\text{O}$  accessing multiple hydrogen-bonding sites on the acid. The most intense absorption bands are assigned to the local minimum structures stabilized by a single non-classical HB formation. The calculated interaction energies along with interconversion barriers between isomers clearly depicted the kinetic trapping of species at 0.4 K, a phenomenon commonly observed in helium droplets. These findings highlight the competing roles of dipole-dipole and higher-order interactions in directing complex formation at ultracold temperatures. The substantial dipole moments of  $\text{D}_2\text{O}$  (1.85 D) and PA (1.59 D) promote long-range directional hydrogen bonding, which is subsequently complemented by short-range stabilization through the most favorable hydrogen-bonding interactions upon contact.



## Author contributions

A. C. has designed and carried out the experiments and computations. M. H. has set-up a helium droplet experiment in Bochum, managed the project and provided funding. Data analysis and interpretation were carried out by A. C., G. S., and M. H. S. H. has contributed to mathematical analysis. All authors participated in the preparation and proofreading of the manuscript.

## Conflicts of interest

There is no conflict to declare.

## Data availability

The data generated in this study have been deposited in our open-access repository: <https://doi.org/10.17877/RESOLV-2025-MF12V240>.

Supplementary information (SI): pressure dependent pick-up curves for the IR bands of the propiolic acid (PA) monomer and PA $\cdot\cdot$ D<sub>2</sub>O dimers, comparison of the IR spectra of PA $\cdot\cdot$ D<sub>2</sub>O varying the pick-up pressure of D<sub>2</sub>O, calculated anharmonic spectra of PA, and optimized structures and coordinates of possible PA $\cdot\cdot$ D<sub>2</sub>O and PA $\cdot\cdot$ H<sub>2</sub>S dimers are provided. See DOI: <https://doi.org/10.1039/d5cp02794b>.

## Acknowledgements

This work was funded by the Deutsche Forschungsgemeinschaft (DFG, German Research Foundation) under Germany's Excellence Strategy-EXC2033-390677874-RESOLV.

## References

- 1 A. S. N. Murthy and C. N. R. Rao, *Appl. Spectrosc. Rev.*, 1968, **2**, 69.
- 2 S. J. Grabowski, *Chem. Commun.*, 2024, **60**, 6239.
- 3 L. Sobczyk, S. J. Grabowski and T. M. Krygowski, *Chem. Rev.*, 2005, **105**(10), 3513.
- 4 D. Herschlag and M. M. Pinney, *Biochemistry*, 2018, **57**, 3338.
- 5 J. Poater, M. Swart, C. Fonseca Guerra and F. M. Bickelhaupt, *Chem. Commun.*, 2011, **47**(26), 7326.
- 6 A. Chakraborty, T. Brumme, S. Schmahl, H. Weiske, C. Baldauf and K. R. Asmis, *Chem. Sci.*, 2022, **13**(44), 13187.
- 7 Y. Liu, L. Wang, L. Zhao, Y. Zhang, Z.-T. Li and F. Huang, *Chem. Soc. Rev.*, 2024, **53**(3), 1592.
- 8 S. E. Harold, C. J. Bready, L. A. Juechter, L. A. Kurfman, S. Vanovac, V. R. Fowler, G. E. Mazaleski, T. T. Odbadrakh and G. C. Shields, *J. Phys. Chem. A*, 2022, **126**(10), 1718.
- 9 M. Conroy, J. A. Soltis, R. S. Wittman, F. N. Smith, S. Chatterjee, X. Zhang, E. S. Ilton and E. C. Buck, *Sci. Rep.*, 2017, **7**(1), 13274.
- 10 M. Tahmasebpour, L. de Martín, M. Talebi, N. Mostoufi and J. R. van Ommen, *Phys. Chem. Chem. Phys.*, 2013, **15**(16), 5788.
- 11 L. A. Galuska, M. U. Ocheje, Z. C. Ahmad, S. Rondeau-Gagné and X. Gu, *Chem. Mater.*, 2022, **34**(5), 2259.
- 12 Y. Liu, Y. Deng, J. Zheng, F. Wu, J. Lu, S. Sun, D. Wu and T. Wu, *Sol. Energy Mater. Sol. Cells*, 2022, **248**, 112031.
- 13 E. Arunan, G. R. Desiraju, R. A. Klein, J. Sadlej, S. Scheiner, I. Alkorta, D. C. Clary, R. H. Crabtree, J. J. Dannenberg, P. Hobza, H. G. Kjaergaard, A. C. Legon, B. Mennucci and D. J. Nesbitt, *Pure Appl. Chem.*, 2011, **83**(8), 1637.
- 14 S. Civiš, M. Lamanec, V. Špirko, J. Kubišta, M. Špet'ko and P. Hobza, *J. Am. Chem. Soc.*, 2023, **145**(15), 8550.
- 15 K. Chatterjee, T. K. Roy, J. Khatri, G. Schwaab and M. Havenith, *Phys. Chem. Chem. Phys.*, 2021, **23**(25), 14016.
- 16 A. Gutiérrez-Quintanilla, M. Briant, E. Mengesha, M.-A. Gaveau, J.-M. Mestdagh, B. Soep and L. Poisson, *Low Temp. Phys.*, 2019, **45**(6), 634.
- 17 I. Alkorta, I. Rozas and J. Elguero, *Chem. Soc. Rev.*, 1987, **27**, 163.
- 18 M. Ortlieb, O. Birer, M. Letzner, G. W. Schwaab and M. Havenith, *J. Phys. Chem. A*, 2007, **111**(49), 12192.
- 19 S. Jäger, J. Khatri, P. Meyer, S. Henkel, G. Schwaab, A. Nandi, P. Pandey, K. R. Barlow, M. A. Perkins, G. S. Tschumper, J. M. Bowman, A. van der Avoird and M. Havenith, *Nat. Commun.*, 2024, **15**(1), 9540.
- 20 R. Schwan, M. Kaufmann, D. Leicht, G. Schwaab and M. Havenith, *Phys. Chem. Chem. Phys.*, 2016, **18**(34), 24063.
- 21 A. Metzethin, O. Birer, E. Sánchez-García and M. Havenith, *J. Chem. Phys.*, 2008, **129**(11), 114307.
- 22 G. R. Desiraju and T. Steiner, *The weak hydrogen bond in structural chemistry and biology, Monographs on crystallography*, Oxford University Press, Oxford, 1st edn, 2001, p. 9.
- 23 Y. Wang, Y. Zhao, X. Xu, W. Gao, Q. Zhang and W. Huang, *Batteries Supercaps*, 2024, **7**(12).
- 24 D. Cappelletti, A. Bartocci, F. Frati, L. F. Roncaratti, L. Belpassi, F. Tarantelli, P. A. Lakshmi, E. Arunan and F. Pirani, *Phys. Chem. Chem. Phys.*, 2015, **17**(45), 30613.
- 25 M. Goswami and E. Arunan, *Phys. Chem. Chem. Phys.*, 2009, **11**(40), 8974.
- 26 Z. Xue and M. A. Suhm, *Mol. Phys.*, 2010, **108**(17), 2279.
- 27 A. J. Barnes and Z. Mielke, *J. Mol. Struct.*, 2012, **1023**, 216.
- 28 L. George and W. Sander, *Spectrochim. Acta, Part A*, 2004, **60**(13), 3225.
- 29 K. Nauta and R. E. Miller, *Science*, 1999, **283**, 1895.
- 30 S. Yang and A. M. Ellis, *Chem. Soc. Rev.*, 2013, **42**(2), 472.
- 31 F. Madeja, M. Havenith, K. Nauta, R. E. Miller, J. Chocholousová and P. Hobza, *J. Chem. Phys.*, 2004, **120**(22), 10554.
- 32 J. A. Davies, M. W. D. Hanson-Heine, N. A. Besley, A. Shirley, J. Trowers, S. Yang and A. M. Ellis, *Phys. Chem. Chem. Phys.*, 2019, **21**(26), 13950.
- 33 A. Chakraborty, S. Henkel, G. Schwaab and M. Havenith, *J. Phys. Chem. A*, 2024, **128**(27), 5307.
- 34 J. D. Pickering, B. Shepperson, L. Christiansen and H. Stapelfeldt, *J. Chem. Phys.*, 2018, **149**(15), 154306.
- 35 K. Nauta and R. E. Miller, *Science*, 2000, **287**, 293.
- 36 D. Mani, N. Pal, M. Smialkowski, C. Beakovic, G. Schwaab and M. Havenith, *Phys. Chem. Chem. Phys.*, 2019, **21**(37), 20582.



- 37 A. Kumar, H. P. Upadhyaya, P. D. Naik, D. K. Maity and J. P. Mittal, *J. Phys. Chem. A*, 2002, **106**(49), 11847.
- 38 S. Lopes, T. Nikitin and R. Fausto, *J. Phys. Chem. A*, 2019, **123**(8), 1581.
- 39 B. A. Shiekh and D. Kaur, *Chem. Phys. Lett.*, 2016, **646**, 168.
- 40 E. Isoniemi, L. Khriachtchev, M. Makkonen and M. Räsänen, *J. Phys. Chem. A*, 2006, **110**(40), 11479.
- 41 J. Bournay and Y. Maréchal, *J. Chem. Phys.*, 1971, **55**(3), 1230.
- 42 F. Gao, S. Aminane, S. Bai and A. V. Teplyakov, *Chem. Mater.*, 2017, **29**(9), 4063.
- 43 E. M. N. Ndip, PhD thesis, Texas Tech University, 1987, <https://hdl.handle.net/2346/9876>.
- 44 H. S. Biswal, S. Bhattacharyya, A. Bhattacharjee and S. Wategaonkar, *Int. Rev. Phys. Chem.*, 2015, **34**(1), 99.
- 45 D. Mani, T. Fischer, R. Schwan, A. Dey, B. Redlich, A. F. G. van der Meer, G. Schwaab and M. Havenith, *RSC Adv.*, 2017, **7**(86), 54318.
- 46 M. Lewerenz, B. Schilling and J. P. Toennies, *J. Chem. Phys.*, 1995, **102**(20), 8191.
- 47 M. J. Frisch, M. Head-Gordon and J. A. Pople, *Chem. Phys. Lett.*, 1990, **166**(3), 275.
- 48 T. H. Dunning, *J. Chem. Phys.*, 1989, **90**(2), 1007.
- 49 M. Gray, P. E. Bowling and J. M. Herbert, *J. Chem. Theory Comput.*, 2022, **18**(11), 6742.
- 50 S. F. Boys and F. Bernardi, *Mol. Phys.*, 1970, **19**(4), 553.
- 51 S. Grimme, J. Antony, S. Ehrlich and H. Krieg, *J. Chem. Phys.*, 2010, **132**(15), 154104.
- 52 M. J. Frisch, G. W. Trucks, H. B. Schlegel, G. E. Scuseria, M. A. Robb, J. R. Cheeseman, G. Scalmani, V. Barone, G. A. Petersson, H. Nakatsuji, X. Li, M. Caricato, A. V. Marenich, J. Bloino, B. G. Janesko, R. Gomperts, B. Mennucci, H. P. Hratchian, J. V. Ortiz, A. F. Izmaylov, J. L. Sonnenberg, D. Williams-Young, F. Ding, F. Lipparini, F. Egidi, J. Goings, B. Peng, A. Petrone, T. Henderson, D. Ranasinghe, V. G. Zakrzewski, J. Gao, N. Rega, G. Zheng, W. Liang, M. Hada, M. Ehara, K. Toyota, R. Fukuda, J. Hasegawa, M. Ishida, T. Nakajima, Y. Honda, O. Kitao, H. Nakai, T. Vreven, K. Throssell, J. A. Montgomery Jr., J. E. Peralta, F. Ogliaro, M. J. Bearpark, J. J. Heyd, E. N. Brothers, K. N. Kudin, V. N. Staroverov, T. A. Keith, R. Kobayashi, J. Normand, K. Raghavachari, A. P. Rendell, J. C. Burant, S. S. Iyengar, J. Tomasi, M. Cossi, J. M. Millam, M. Klene, C. Adamo, R. Cammi, J. W. Ochterski, R. L. Martin, K. Morokuma, O. Farkas, J. B. Foresman and D. J. Fox, Gaussian Inc., Wallingford CT, 2016.
- 53 A. M. Ellis, J. A. Davies, E. Yurtsever and F. Calvo, *J. Chem. Phys.*, 2022, **156**(17), 174304.
- 54 A. Metzethin, E. Sánchez-García, Ö. Birer, G. Schwaab, W. Thiel, W. Sander and M. Havenith, *ChemPhysChem*, 2011, **12**(10), 2009.

